COBEM 2023 · 27TH INTERNATIONAL CONGRESS OF MECHANICAL ENGEENERING

ABCM · Brazilian Society of Mechanical Sciences and Engineering
27th ABCM International Congress of Mechanical Engineering
December 04-08, 2023, Florianópolis-SC, Brazil

COB-2023-2056
MESH GENERATION METHODOLOGY FOR NUMERICAL SIMULATION OF FLOW WITHIN MULTILOBE PROGRESSING CAVITY PUMPS

Tulio Rafael Nascimento Porto
João Alves de Lima
Federal University of Paraíba - PPGEM/CT/UFPB & DEER/CEAR/UFPB
João Pessoa/PB, Brazil.
trnp@academico.ufpb.edu.br; jalima@cear.ufpb.br

Tony Hebert Freire de Andrade
Tales Dmitre Araújo Lopes
Federal University of Campina Grande, Department of Petroleum Engineering
Campina Grande/PB, Brazil.
tonyherbert@uaepetro.ufcg.edu.br

***Abstract.** The success of a tool in oil production depends on understanding the physical phenomena involved in its operation. Multi-lobe Progressive Cavity Pumps (PCPs) are extensions of traditional mono-lobe PCPs designed to operate with high oil flow rates. Due to the geometric complexity related to the flow inside these machines, most attempts to describe the fluid dynamics of multilobe PCPs use simplified models, which do not consider the details of the turbulent, three-dimensional and transient flow that occurs inside these pumps. In this sense, this work proposes a methodology for generating moving and deformable meshes with optimized topologies to be used in computational simulations of flows within multilobe PCPs. The mesh generation presented in this work was developed in Fortran 90 language, which can be used as a dynamic library to be executed in the Ansys CFX® software or as an independent program. The results developed for the 3-4 PCP, demonstrate that the methodology is able to produce structured meshes centered on the stator center, at each time-step, following the pump's kinematics. Unlike other methodologies developed to analyze multilobe PCPs, this work proposes a mesh generation method that is run internally in the CFX® calculation kernel, without the need to reading external files of previously generated meshes, which is the common practice in other works.*

***Keywords:** Multilobe Progressing Cavity Pump, Structured Mesh Generation, 3D- Unsteady Computational Simulation.*

1. INTRODUCTION

Some oil wells produce extremely viscous and dense mixtures of oil, water, gas, and occasionally sand, natural gas hydrates, and waxes. To transport this mixture to a central processing facility, the application of flow machines is necessary, capable of ensuring a flow that is described by a complexity of associated physical phenomena such as turbulence, vibrations, fluid emulsion, and erosion of solid particles.

The Progressive Cavity Pump (PCP) was invented in the late 1920s by the French engineer René Joseph Louis Moineau. These pumps consist of two elements: a metallic rotor and an elastomeric (or metallic) stator. When the rotor rotates inside the stator, the fluid moves along the pump's axis within sealed cavities located between the rotor and the stator (Gravesen, 2008). Unlike positive displacement pumps, the flow rate of a PCP is not pulsating but constant and proportional to the rotor's rotational speed. Furthermore, this flow rate depends on the rotor diameter, pump eccentricity, and stator pitch length. Additionally, the lifting capacity or nominal head of a PCP depends on the number of stator cavities (the total length of the pump).

A multi-lobe Progressive Cavity Pump (PCP) is the generalized case of the mono-lobe PCP, whose relation between the number of lobes of the rotor (N_r) ≥ 1 and the number of lobes of the stator (N_e) is $N_e = N_r + 1$. These pumps are described as "$N_r - N_e$ PCPs". Additionally, the pitch relationship is established as follows:

$$Pas_e = \frac{N_r+1}{N_r} Pas_r \qquad (1)$$

For example, for a 3-4 multilobe PCP, the stator pitch will be 4/3 times the rotor pitch, which represents a reduction in pitch ratio compared to the 1-2 mono-lobe PCP.

According to Wittrisch & Cholet (2012), multilobe PCPs exhibit an increased flow capacity corresponding to an increase in the number of lobes due to higher fluid displacement inside the PCP. They also have a lower value of eccentricity (E), which represents lower rotor imbalances, vibrations, and dimensions of the eventual connection to the drive shaft. Additionally, multilobe PCPs have a reduction in the positive suction load per cavity generated due to a larger number of sealing lines separating the cavities. As a result, for the same pump length, it is possible to increase the total positive suction load by increasing the number of lobes in the PCP.

Gamboa *et al.* (2003a) modeled the performance of monolobe PCPs by considering two flow leakage components: one due to the rotor movement and another due to the differential pressure between the cavities, assuming that the flow area depends on the stator material. They highlighted that the internal deformation of the stator is the main parameter to be understood before predicting the performance of PCPs.

Paladino *et al.* (2008, 2009, 2011) and Pessoa *et al.* (2009) presented a computational model for 3D and transient flow in monolobe PCPs. In contrast to previous models, these studies succeeded in developing a mesh generator for monolobe PCPs, enabling accurate prediction of operational parameters such as volumetric efficiency and viscous losses. They also obtained detailed information about the pressure and velocity fields of single-phase flow inside the pump, which was validated against experimental data.

Almeida (2010) developed a transient three-dimensional computational model for analyses of the dynamic fluid-structure interaction (FSI) process that occurs inside metallic and elastomeric PCPs. Assmann (2011) developed a methodology for mesh generation for an elastomeric monolobe PCP with interference. In these cases, the interference between the rotor and the stator is dynamic, following the position of the rotor within the pump.

De Azevedo *et al.* (2016) employed the mesh generator process developed by Almeida (2010) and performed a CFD analysis for the transient, three-dimensional two-phase flow inside a monolobe PCP. The model accurately predicted volumetric efficiency and viscous losses, providing detailed information on pressure and velocity fields, as well as void distribution along the pump. Gas compressibility was taken into account, and the effects of different gas volume fractions (GVFs) on pump volumetric efficiency, pressure distribution, power, slip flow rate, and volumetric flow rate were analyzed.

Nguyen *et al.* (2014) employed a three-dimensional vector formulation and the mathematical equations of hypocycloids to develop a geometric modeling of multilobe PCPs. The authors presented a mathematical model to determine the theoretical single-phase pumping factor for any type of rotor-stator configuration.

Nguyen *et al.* (2016) developed a model to predict the actual performance of multilobe PCPs and evaluated the pump's performance through simulations of single-phase flows inside it. The authors concluded that viscosity, in most cases, minimizes pump slip, and if the pump clearance is smaller than a specific value, the effects of differential pressure and liquid viscosity on pump performance are minimal.

Al-Safran *et al.* (2017) stablished a set of dimensionless groups that govern fluid flow behavior in a PCP capable of predicting pressure drop for different pump velocities with 85% accuracy. Zheng *et al.* (2018) develops an analytical model to simulate the flow inside single-lobe PCPs, based on the similitude between the gear and PCP dynamics, considering the pump clearance geometries.

El-Abd *et al.* (2020) developed a detailed numerical procedure to simulate single-phase flow in multilobe PCPs with a metallic stator, transporting viscous oils. The authors applied profile equations for the multilobe configuration at any section and at each rotational instant, following the mathematical model of the pump geometry presented by Nguyen *et al.* (2014), while incorporating the effects of eccentricity, rolling, and clearance in the equations. Additionally, they applied a method for generating structured meshes based on the works of Paladino *et al.* (2008, 2009, 2011) and Pessoa *et al.* (2009). With this approach, the authors were able to investigate the effect of geometric parameters on pump efficiency.

In this work, the objective is to develop a mesh generation methodology for multilobe PCPs, based on the ideas of these previous works, to be applied in transient simulations within the commercial fluid dynamics software Ansys CFX®. The proposal consists of creating an interactive system that internally calculates, in the CFX® solver kernel, the meshes for each time-step of the PCP's operation, without the need to store them in external files for posterior reading, which is usually adopted in PCP multilobe analyses developed to date. With this mesh generation methodology, it will be possible to automatically perform simulations of two-way fluid-structure interaction, dynamically adapting the geometric variations that the stator may undergo during pump operation and its effect on the flow and structural field.

2. KINEMATICS OF MULTI-LOBE PCPS

In order to map the positions of the PCP throughout the studied time steps, it is necessary to define the geometric parameters that describe the pump's kinematics. For this purpose, a mathematical model needs to be developed to determine the curves that characterize the geometry of the cross-sectional profiles of the rotor and stator in multilobe PCPs. As described in Figure 1, for the geometry of a 3-4 multilobe PCP, these curves can be described by semicircles (lobes) and modified hypocycloid curves (intervals between the lobes). With this modeling approach, parametric curves of the positions (x, y) of the points on the surfaces of the rotor and stator can be obtained at each "z" section along the length of the PCP, based on the pump's rotation, the helix angle of the rotor and stator, and the eccentricity of the rotor.
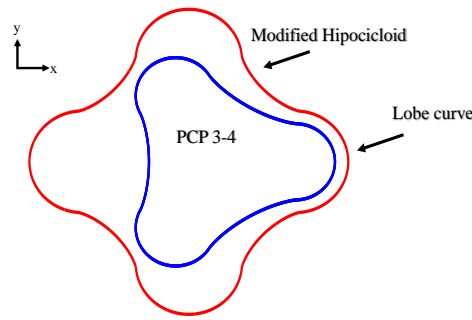
Figure 1. Characteristic curve of the 3-4 PCP.

2.1 Original and Modified Hypocycloid

Figure 2a illustrates the development of the two-dimensional curve called a 4-cusped hypocycloid. This curve describes the path of a point P located on the generating circle with radius r (C_g) and center C_1, which rotates clockwise rolling within a base circle (C_B) of radius R and center O. This rotational movement describes an angle θ in the base circle counterclockwise, marking the angular position of point C_1 relative to the center O. At the same time, it describes an arc of angle ϕ, marking the angular position of point P relative to the center C_1. Taking values of θ ranging from 0 to 2π, a closed curve is generated in the shape of a hypocycloid with the number of cusps equal to N (4 for the illustrated case).
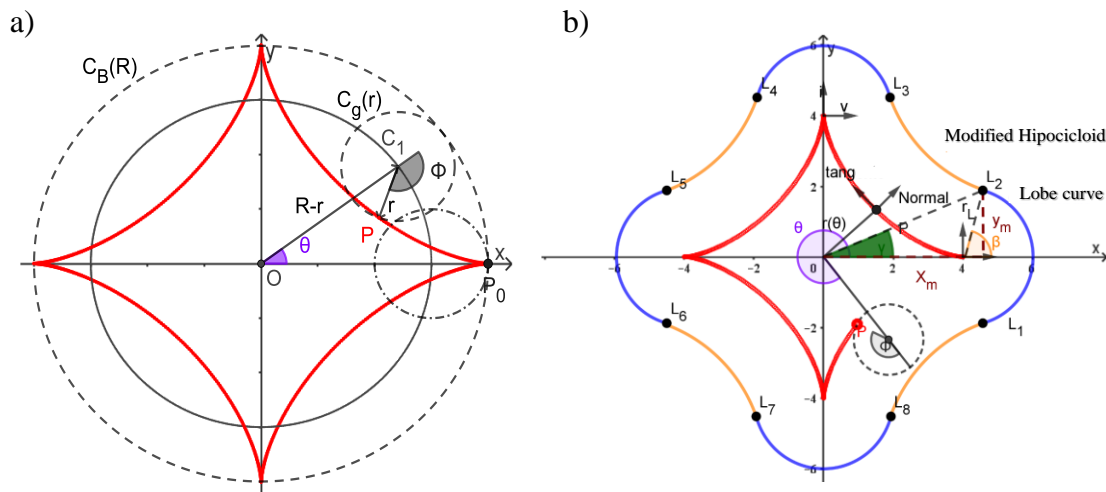

Figure 2. a) 4-Cusped Hypocycloid Curve b) Modified Hypocycloid Curve and Lobe Curve

In Figure 2b, the angle γ is illustrated, which represents the angular position of point P relative to the center O. This angle differs from the angle θ, which measures the angular position of point C_1. The modified hypocycloid curve, depicted in Figure 2b in orange, is obtained by displacing the original hypocycloid curve by a value of r_L in the direction of the normal vector to the curve.

Now, by taking the second derivative with respect to θ of the equations of the original hypocycloid (Nguyen *et al.*, 2014), we obtain the normal component which, when added in their respective directions to the original equation, yields the equation of the modified hypocycloid:

$$x_m = r\left[(N-1)\cos\theta_1 + \cos\theta_2\right] + \frac{\cos\theta_1 - \cos\theta_2}{\sqrt{2[1-\cos(N\theta)]}} r_L \tag{2}$$

$$y_m = r\left[(N-1)\operatorname{sen} - \operatorname{sen}\theta_2\right] + \frac{\operatorname{sen}\theta_1 - \operatorname{sen}\theta_2}{\sqrt{2[1-\cos(N\theta)]}} r_L \tag{3}$$

$$\theta_1 = \theta \tag{4}$$

$$\theta_2 = (N-1)\theta \tag{5}$$

Figure 2b also illustrates the lobe curve, which is a semicircle centered at the cusps of the original hypocycloid with a sweep angle β that marks the angular boundaries between the lobe and the modified hypocycloid curve. It should be

noted that this angle also differs from the angle γ that marks the angular positions of the points (x, y) on the lobe curve relative to the center O. Considering the equation of the original hypocycloid for the cusp angles (γ_L), the centers of the semicircles of the lobe curves can be obtained. At these centers, the angles β are varied between the limits L to generate the lobe curve. The parametric equations that determine the points of the lobe curve are described as follows:

$$x_L = r(N-1)\cos\gamma_L + r\cos(\gamma_L(N-1)) + r_L \cos(\beta + \gamma_L) \tag{6}$$

$$y_L = r(N-1)\text{sen}\gamma_L - r\,\text{sen}(\gamma_L(N-1)) + r_L \,\text{sen}(\beta + \gamma_L) \tag{7}$$

2.2 Helical and Eccentricity Effects

The geometry of the progressive cavity pump develops in the axial direction following a helical motion. As a result, the positions of the rotor and stator are rotated along the sections in the z-direction. Therefore, the developed mathematical equations (x_m, y_m, and x_L, y_L) need to be modified with respect to the helix angle, θ_z, which is formed counterclockwise and is defined by Eq. (8), where P_{as} is the stator helix pitch value and z is the axial position.

$$\theta_z = 2\pi \frac{z}{P_{as}} \tag{8}$$

Figure 3a shows that the angular position of C_1 relative to the center of the base circle O becomes $\theta + \theta_z$, and the angular position of point P relative to the center C_1 is $\phi - \theta_z$. Therefore, taking into consideration the helical effect, the coordinates of point P defined by the equations of the modified hypocycloid become (El-Abd *et al.*, 2020):

$$x_m = r(N-1)\cos(\theta + \theta_z) + r\cos((N-1)\theta - \theta_Z) \tag{9}$$

$$y_m = r(N-1)\text{sen}(\theta + \theta_z) - r\,\text{sen}((N-1)\theta - \theta_Z) \tag{10}$$

$$x_L = r(N-1)\cos(\gamma_L + \theta_z) + r\cos((N-1)\gamma_L - \theta_Z) + r_L \cos(\beta + \gamma_L + \theta_z) \tag{11}$$

$$y_L = r(N-1)\text{sen}(\gamma_L + \theta_z) - r\,\text{sen}((N-1)\gamma_L - \theta_Z) + r_L \,\text{sen}(\beta + \gamma_L + \theta_z) \tag{12}$$
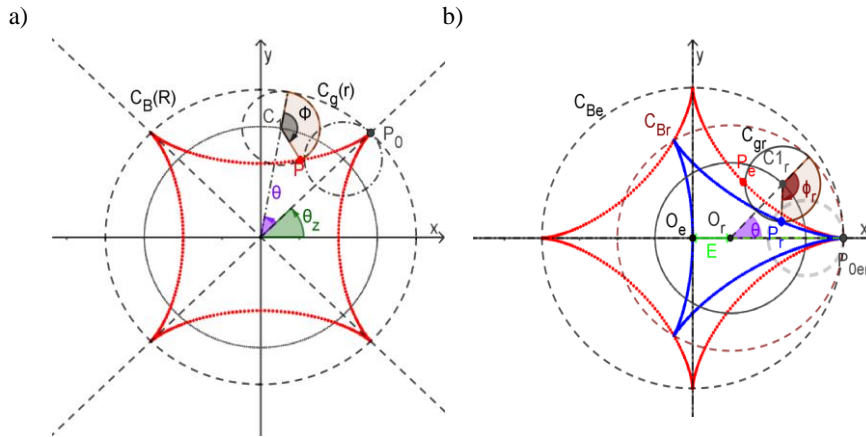

Figure 3. a) Helical Effect, b) Eccentricity Effect

The previous equations describe only the stator geometry, but they cannot be directly applied to generate the rotor geometry due to its eccentric motion relative to the stator. The eccentricity effect is illustrated in Figure 3b, with the Ne=4 hypocycloid (in red) representing the stator with center at $O_e = (0,0)$, and the $N_r = 3$ hypocycloid (in blue) representing the rotor with center at $O_r = (E,0)$. Here, "E" represents the eccentricity value, which is equal to the radius of the generating circle (C_{gr}) of the hypocycloid curve relative to the rotor. Following a similar deduction for N = 4, the curve developed for the rotor is described by an angle θ_r that varies counterclockwise from 0 to 360 degrees and an angle $\phi_r = N\theta_r$ clockwise, producing the rotation of point P_r and describing the curve for the rotor displaced from the center O_e by the value of E.

2.3 Rotor Rolling Effect

During the operation of the PCP, the rotor's base circle (C_{Br}) rotates within the stator's base circle (C_{Be}). Similar to internal gears, the operation of the PCP causes the rotor to rotate around its center (O_r) in a clockwise direction and around the stator's center (O_e) in a counterclockwise direction due to the rotor's eccentricity. These two simultaneous movements

result in the rolling effect of the rotor in relation to the stator.

As illustrated in Figure 4a, the constant angular velocity (ω) of the rotor moves the base circle C_{Br} in a clockwise direction, causing the center C_{1r} and point P_{0r}, which were initially at an angular position of 0 degrees relative to the center O_r at time t = 0s, to be displaced in a clockwise direction by the angle $\omega t/N_r$. Additionally, the rotor's eccentricity displaces the center (O_r) of the base circle C_{Br} relative to the center O_e in a counterclockwise direction by an angle ωt (El-Abd *et al.*, 2020). Figure 4b illustrates the hypocycloid curves of the stator and rotor relative to the rolling motion within the stator, based on the new positions of the rotor's center and point P_{0r}, which is the point Pr corresponding to the angle $\theta_r = 0°$ where the rolling process of the rotor's generating circle C_{gr} begins, resulting in the curve illustrated in blue.
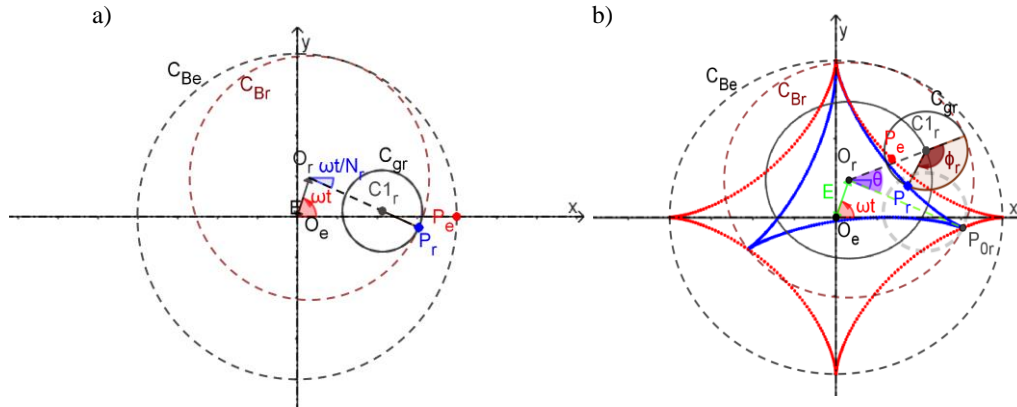

Figure 4. a) The Rotor Rolling Effect on the Stator's Base Circle, b) Hypocycloid Curves of the Stator and Rotor relative to the rolling motion.

Figure 5a depicts the position at the start of the sweep angle θ_r, now due to the helix angle θ_z of the rotor. Similarly, to the stator, this effect results in an increase in counterclockwise angles (θ_r and ϕ_r) that will be developed to construct the hypocycloid curve at this rotor position z. With respect to the center C_{1r}, there is an increase of θ_z in the counterclockwise direction relative to the center O_e, and in contrast, a decrease of θ_z in ϕ_r due to it being developed in the opposite direction. Figure 5b illustrates the rotor and stator hypocycloid curves in relation to the rotor's helix effect.
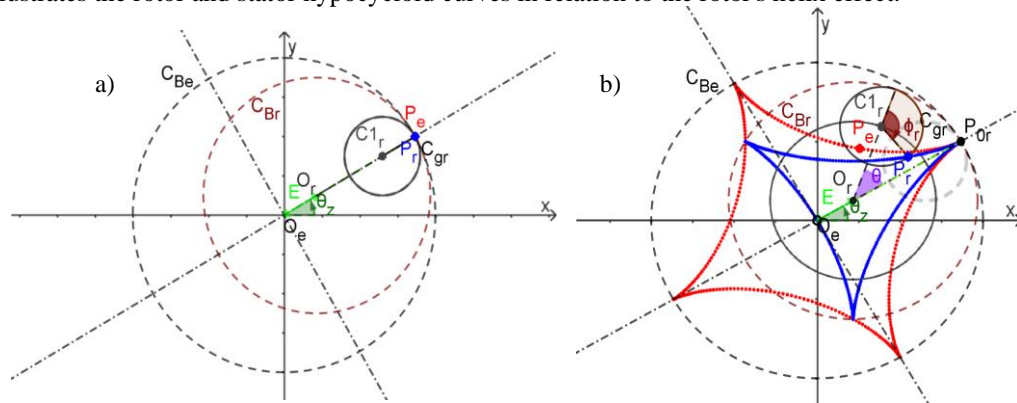

Figure 5. a) Rotor Rolling Effect on the Stator's Base Circle b) Hypocycloid Curves with the Rotor's Helix Effect on the Stator's Base Circle.

Figure 6a shows the movement of the center O_r of the rotor's base circle (C_{Br}) in relation to the center O_e of the stator's base circle (C_{Be}) when the rolling and helix movements are combined for the rotor.

Regarding the rolling effect, it can be observed that the point P_{0r}, from which the movement of the rotor's generating circle (C_{gr}) begins, is displaced by an angle $\omega t/N_r$ in a clockwise direction relative to the center C_{1r}, while the center O_r is displaced by the angle ωt in a counterclockwise direction relative to the center O_e. In addition to this effect, there is the helix effect, which results in an increase of θ_z in the counterclockwise direction in the angular position of the center C_{1r} relative to the center O_e, and a decrease of θ_z in the angular position of the point P_{0r} relative to the center C_{1r}. The point P_{0r} is the starting point from which the angle ϕ_r, representing the rolling of the rotor's generating circle C_{gr} in a clockwise direction, is measured. Figure 6b illustrates the rotor and stator hypocycloid curves in relation to the combined effect of the rotor's helix and rolling effects.

Figure 6. a) Rotor Rolling and Eccentricity Effect on the Stator's Base Circle b) Hypocycloid Curves with the Rotor's Helix and Rolling Effect on the Stator's Base Circle.

Equations 13 to 16 describe the positions of the modified hypocycloid curves and lobes, considering the effects of eccentricity, rolling, helix, and rotor-stator clearance (El-Abd *et al.*, 2020). In the equations, the pump clearance c is subtracted from the lobe radius value (r_L). These equations can be applied to the rotor, with E = r and N = Nr, or to the stator, with E = 0, ωt = 0, and N = N_e.

$$x_m = E\cos(\omega t) + \cos(\theta_Z) + r\big((N-1)\cos\theta_1 + \cos\theta_2\big) + \frac{\cos\theta_1 - \cos\theta_2}{\sqrt{2(1-\cos\cos(N\theta))}}(r_L - c) \tag{13}$$

$$y_m = E\,\text{sen}(\omega t) + \text{sen}(\theta_Z) + r\big((N-1)\text{sen}\theta_1 - \text{sen}\theta_2\big) + \frac{\text{sen}\theta_1 - \text{sen}\theta_2}{\sqrt{2(1-\cos\cos(N\theta))}}(r_L - c) \tag{14}$$

$$x_L = E\cos(\omega t) + \cos(\theta_Z) + r(N-1)\cos(\theta_{1L}) + r\cos(\theta_{2L}) + (r_L - c)\cos(\beta + \theta_{1L}) \tag{15}$$

$$y_L = E\,\text{sen}(\omega t) + \text{sen}(\theta_Z)\; r(N-1)\text{sen}(\theta_{1L}) - r\,\text{sen}(\theta_{2L}) + (r_L - c)\,\text{sen}(\beta + \theta_{1L}) \tag{16}$$

Where

$$\theta_{1L} = \gamma_L + \theta_Z - \frac{\omega t}{N_r} \tag{17}$$

$$\theta_{2L} = (N-1)\gamma_L - \theta_Z + \frac{\omega t}{N_r} \tag{18}$$

3. MESH GENERATION METHOD FOR MULTI-LOBE PCPS

The first step in the mesh generation method is to determine the boundaries of the modified hypocycloid curves and the lobe that describe the geometry of the stator or the rotor, as illustrated in Figure 7.

Figure 7. Boundaries of the Modified Hypocycloid Curves and the Lobe

Therefore, Eqs. (13) and (14) should be used to find the intersection point with the lobe circle defined between L_1 and L_2, with a center at $(x_0, y_0) = (R, 0)$, which is chosen for geometric convenience and aligned with the x-axis. However, other lobes could also be chosen.

The equation of this circle in Cartesian coordinates is defined as follows:

$$(x - x_0)^2 + (y - y_0)^2 = (r_L - c)^2 \qquad (19)$$

By substituting Eqs. (13) and (14) into Eq. (19), we obtain the following nonlinear transcendental equation:

$$(x_m(\theta) - x_0)^2 + (y_m(\theta) - y_0)^2 - (r_L - c)^2 = 0 \qquad (20)$$

By solving this equation using an implicit iterative method, we start with an initial guess θ_0 and calculate a new angle θ_i until the difference between these angles is below the established error. Thus, we obtain the value of θ (L_2), which, when inserted back into Eqs. (13) and (14), determines the points xm_{L2} and ym_{L2} that define the intersection point between the hypocycloid and lobe curves. Applying these values in Eqs. (21) and (22), we have:

$$\gamma_{L_2} = tg^{-1}\left(\frac{y_{mL_2}}{x_{mL_2}}\right) \qquad (21)$$

$$\beta_{L_2} = sen^{-1}\left(\frac{y_{mL_2}}{r_L}\right) \qquad (22)$$

With the value of $\beta_{(L2)}$ and $-\beta_{(L2)}$, we have the limits of the variable β to be inserted into the lobe equations to determine the limits of each lobe. In other words, by applying β_{L2} and β_{L2} to each angle of the lobe γ_L, which is a function of the specific type of PCP and the component (stator or rotor) being considered, we obtain all the points (x_{Ln}, y_{Ln}) corresponding to the boundary angles. These points are calculated using the following vectorial relation:

$$\gamma_{L_n} = tg^{-1}\left(\frac{y_{L_n}}{x_{L_n}}\right) \qquad (23)$$

With the determined limits, we perform the angular discretization of γ, creating the mesh angle γ_j as follows:

$$NP_{angular} = \left[\frac{(360° - 0°)}{\Delta\gamma}\right] + 1 \qquad (24)$$

$$\gamma_j = (j - 1)\Delta\gamma \qquad (25)$$

For j ranging from 1 to $NP_{angular}$, which is the number of points determined for an angular sweep from 0° to 360°, and with $\Delta\gamma$ determined as an input parameter.

In the regions of the lobes, the nodes on the rotor or stator are intersections between the radial lines (R_0) and the lobe curve within the defined angular limits. Starting from the R_0 equation:

$$R_0: \begin{cases} y = Ax + B \\ A = \tan(\gamma) \\ B = 0 \ (Radial\ line\ centered\ at\ O_e) \end{cases} \qquad (26)$$

And by applying Eqs. (15) and (16) to Eq. (26), we obtain:

$$tg(\gamma)\, x_L(\beta) - y_L(\beta) = 0 \qquad (27)$$

This equation should be solved iteratively so that, at each angle γ of the numerical mesh, the corresponding β can be determined. With the determined β angle, we apply it to Eqs. (15) and (16) to obtain the points (x_e, y_e) for the stator surface, or the points (x_r, y_r) for the rotor surface, which are the intersection points between the radial line R_0 and the lobe curve within the angular interval determined by the limits Ln.

In the regions between the lobes, the nodes on the rotor or stator are intersections between the radial lines (R_0) and the modified hypocycloid curve within the defined angular limits. By applying Eqs. (13) and (14) to Eq. (26), we obtain:

$$tg(\gamma)\, x_m(\theta) - y_m(\theta) = 0 \qquad (28)$$

As before, this equation should be solved iteratively so that, at each angle γ of the numerical mesh, the corresponding θ can be determined. With the determined θ angle, we apply it to Eqs. (13) and (14) to obtain the points (x_e, y_e) for the stator surface, or the points (x_r, y_r) for the rotor surface, which are the intersection points between the radial line R_0 and the modified hypocycloid curve within the angular interval determined by the limits Ln.

With the points (x_e, y_e) on the stator surface and the points (x_r, y_r) on the rotor surface determined, we have, for each angular variation γ of the mesh, the linear intervals between these surfaces, where the moving mesh will be created for each time step of the multilobe PCP operation. By dividing these lines into equally spaced discrete points in the radial direction, we have the discretization of the structured mesh for the PCP (Eqs. 29 and 30) based on the pump's kinematics (for i varying from 1 to $NP_{radial} + 2$, where NP_{radial} is the number of points chosen in the radial direction):

$$x_{radial_i} = x_r(\gamma_j) + (i-1)\Delta x \tag{29}$$

$$y_{radial_i} = y_r(\gamma_j) + (i-1)\Delta y \tag{30}$$

$$\Delta x = \frac{(x_e - x_r)}{NP_{radial} + 1} \tag{31}$$

$$\Delta y = \frac{(y_e - y_r)}{NP_{radial} + 1} \tag{32}$$

Figures 8 and 9 illustrate the mesh generation methodology developed in the previous sections, connecting the geometries of the rotor and stator.

Figure 8a represents the initial time step when the rotor and stator are aligned at $\omega t = \theta_z = 0°$. At this moment, the initial positions of the limits L_{ne} for the stator and L_{nr} for the rotor are observed. Additionally, two radial lines, R_1 intersecting the points P_{1r} (rotor) and P_{1e} (stator), and R_2 intersecting the points P_{2r} (rotor) and P_{2e} (stator), are highlighted. Figure 8b represents the rotor rotating 90° clockwise while the stator remains stationary. It can be observed that the positions of the limits L_{ne} remain the same, and the lines R_1 and R_2 intersect the same points P_{1e} and P_{2e} on the stator curve, respectively. However, for the rotor, the positions of the limits L_{nr} are altered according to the rotation, although the sequence of limits remains the same. Additionally, new points on the rotor surface, P'_{1r} and P'_{2r}, are intersected by the lines R_1 and R_2, respectively. This position changes of points on the rotor surface ensures that the elements constructed from the points on the radial lines are not distorted with the movement of the pump.
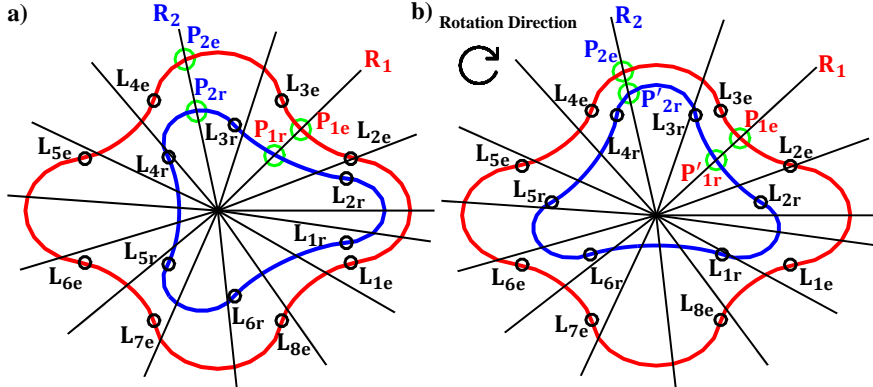

Figure 8. a) Initial position, when the rotor and stator are aligned at $\omega t = \theta_z = 0°$; b) Initial position, when the rotor and stator are aligned at $\omega t = 90°$ $\theta_z = 0°$.
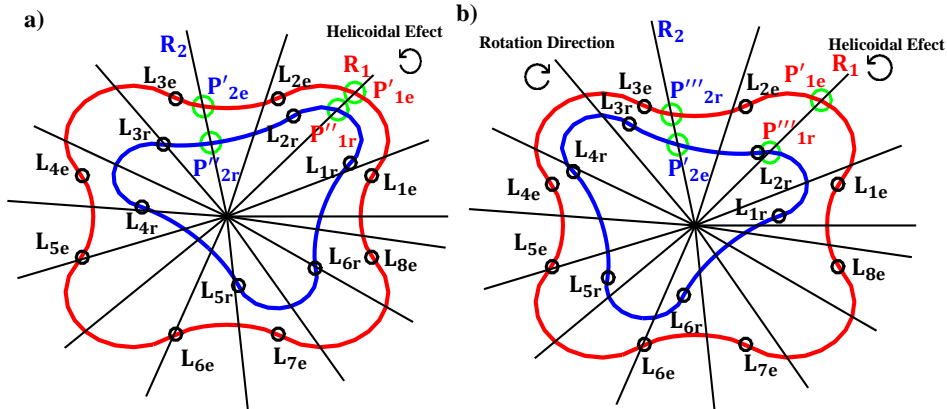

Figure 9. a) Initial position, when the rotor and stator are aligned at $\omega t = 90°$ and $\theta_z = 0°$; b) Initial position, when the rotor and stator are aligned at $\omega t = 0°$ and $\theta_z = 45°$.

Figure 9a corresponds to the position z when the helix angle $\theta_z = 45°$ in the counterclockwise direction. In this position, both the rotor curve and the stator curve are intersected at different points compared to the position $\theta_z = 0°$.

Therefore, the same line R_1 now intersects the points P''_{1r} (rotor) and P'_{1e} (stator), and the same line R_2 intersects the points P''_{2r} (rotor) and P'_{2e} (stator). Figure 9b illustrates the curves of the rotor and the stator at the z position corresponding to the helix angle $\theta_z = 45°$ with the rotor rotated clockwise by 90°. It can be observed that the lines R_1 and R_2 intersect, respectively, the same points P'_{1e} and P'_{2e} on the stator curve. As for the rotor, new points, P'''_{1r} and P''_{2r}, on the surface curve of this component are intersected, respectively, by the lines R_1 and R_2.

4. RESULTS AND DISCUSSION

At the present work development stage, the main goal is to demonstrate capability of the proposed methodology to produce adequate meshes to the analyzed geometry. Therefore, only general meshes will be illustrated as results. Figure 10 illustrates the structured meshes centered on the stator center developed for a 3-4 PCP with a helix angle $\theta_z = 45°$. At each instant of time, the mesh is evaluated according to the pump's kinematics presented in the previous sections. With the same methodology, it is possible to obtain meshes for any multilobe configuration.
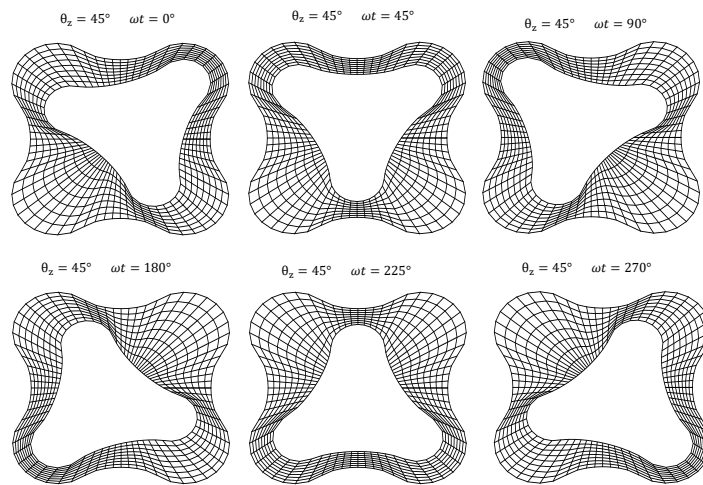

Figure 10. Section $\theta_z = 45°$ and ωt ranging from 0° to 270° of the structured meshes produced for the 3-4 PCP.
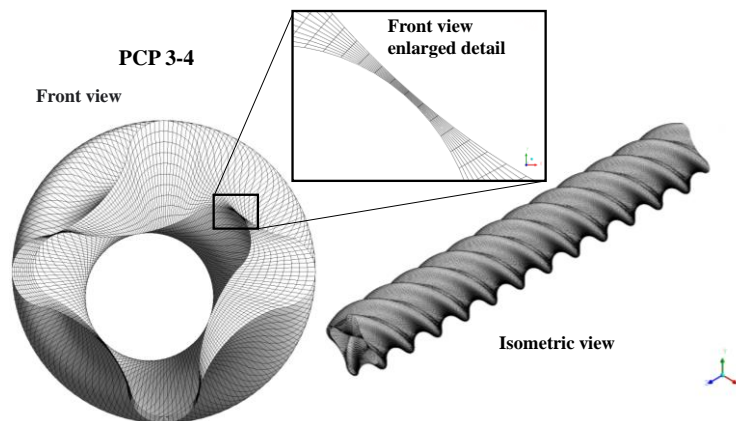

Figure 11. Frontal close-up view of the mesh developed for a 3-4 PCP.
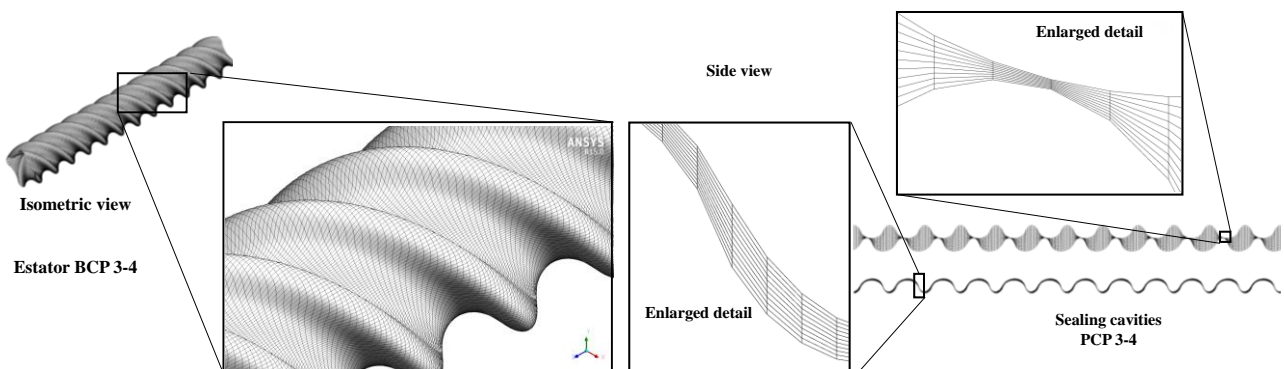

Figure 12. Isometric view and longitudinal section of the sealing lines of the mesh developed for 3-4 PCP.

Figure 11 illustrates the three-dimensional mesh of the 3-4 PCP at time t = 10s, highlighting the fluid domain and the rotor and stator lobes. In Figure 12, there is a detailed view of the surface in an isometric view and a longitudinal cut, highlighting the mesh characteristics near the pump sealing.

The results demonstrate that it was possible to generate moving and deformable structured meshes for multilobe PCPs by calculating the positions of each mesh element at any instant of time. This procedure can be performed internally in the calculation kernel of the Ansys-CFX® without the need to read previously recorded meshes, as applied in previous works reported in the literature. In this way, the time step adopted can be changed according to the analysis objective, without the need to create other meshes. Furthermore, with this methodology it is possible to carry out structural analysis using the previously defined models, without the need to apply another structural analysis software.

5. CONCLUSIONS

The mathematical modeling of the kinematics of multilobe PCPs was able to geometrically describe how the surfaces of these pumps can be modeled by curves known as modified hypocycloids for regions between the lobes, associated with semicircles for regions within the lobes. The present methodology was developed using iterative methods that allowed determining the boundaries of the geometry in which each equation should be used to describe the PCP.

With this methodology, it is possible to calculate the meshes directly inside the commercial package Ansys-CFX® for solving the governing equations that govern the dynamics of turbulent and multiphase fluid flow within multilobe PCPs. Additionally, the developed methodology can be extended to analyze the fluid and structural interactions between the flow field inside the pump and its stator deformations, since the same procedure can be applied to generate the structural stator mesh and a proprietary structural routine can also be run internally on the same mesh generating library.

6. REFERENCES

Almeida, R.F.C., 2010. *Computational Simulation of Fluid-Structure Interaction in Progressive Cavity Pumps*. Master's Thesis, Graduate Program in Mechanical Engineering, Federal University of Rio Grande do Norte, Natal, Brasil.

Al-Safran, E., Aql, A., & Nguyen, T., 2017. Analysis and prediction of fluid flow behavior in progressing cavity pumps. Journal of Fluids Engineering, v.139, n.12, 121102 (11 pages). https://doi.org/10.1115/1.4037057

Azevedo, V.W.F., Lima, J.A., Paladino, E.E., 2016. "A 3D transient model for the multiphase flow in a progressing-cavity pump". SPE Journal, v. 21, n. 04, p. 1458-1469. https://doi.org/10.2118/178924-PA

El-Abd, F.M.; Wahba, E.M., Adam, I.G., 2020. "Viscous flow simulations through multi-lobe progressive cavity pumps. Petroleum Science", v. 17, n. 3, p. 768-780. https://doi.org/10.1007/s12182-020-00458-6

Gravesen, J., 2008. "The geometry of the Moineau pump". Computer Aided Geometric Design, v. 25, n. 9, p. 792-800. https://doi.org/10.1016/j.cagd.2008.06.012

Gamboa, J., Olivet, A., Iglesias, J. Gonzalez, P., 2003. "Understanding the performance of a progressive cavity pump with metallic stator". Proceedings of the 20th International Pump User's Symposium.

Gamboa, J., Aurelio, O., Sorelys, E., 2003. "New approach for modeling progressive cavity pumps performance". SPE Annual Technical Conference and Exhibition, Denver, Colorado, October 2003. Paper: SPE-84137-MS

Paladino, E.E., Lima, J.A., Almeida, R.F.C., Assmann, B.W., "Computational modeling of the three-dimensional flow in a metallic stator progressing cavity pump", SPE Progressing Cavity Pumps Conference, Paper SPE-114110-MS, 2008. https://doi.org/10.2118/114110-MS

Paladino E.E., Lima, J.A., Pessoa, P.A.S., Almeida, R.F.C., 2011. "A computational model for the flow within rigid stator progressing cavity pumps". Journal of Petroleum Science and Engineering, v. 78, n. 1, p. 178-192. https://doi.org/10.1016/j.petrol.2011.05.008

Paladino, E.E., Almeida, R.F.C., Assmann, F.P.M, 2009. "Mesh generation for numerical simulation of fluid-structure interaction within progressing cavity pumps". 20th International Congress of Mechanical Engineering - COBEM, November 15-20, Gramado/RS, Brazil.

Pessoa, P.A.S., Paladino, E.E., Lima, J.A., 2009. "A simplified model for the flow in a progressive cavity pump". 20th International Congress of Mechanical Engineering - COBEM, November 15-20, Gramado/RS, Brazil.

Nguyen, T., Al-Safran, E., Saasen, A., Nes, O-M., 2014. "Modeling the design and performance of progressing cavity pump using 3-D vector approach", J. Pet. Sci. Eng., vol. 122, pp. 180-186. https://doi.org/10.1016/j.petrol.2014.07.009

Nguyen, T., Tu, H., Al-Safran, E., Saasen, A., 2016. "Simulation of single-phase liquid flow in Progressing Cavity Pump", J. Pet. Sci. Eng., v. 147, p. 617-623. https://doi.org/10.1016/j.petrol.2016.09.037

Wittrisch, C., Cholet, H., 2012. "Progressing Cavity Pumps: Oil Well Production Artificial Lift", Technip Editions, Paris.

Zheng, L., Wu, X., Han, G., Li, H., Zuo, Y., & Zhou, D., 2018. Analytical model for the flow in progressing cavity pump with the metallic stator and rotor in clearance fit. Mathematical Problems in Engineering, 2018.

7. RESPONSIBILITY NOTICE

The authors are the only responsible for the printed material included in this paper.